Available online at www.sciencedirect.com

ScienceDirect

Ceramics International 40 (2014) 2825–2834

CERAMICS INTERNATIONAL

www.elsevier.com/locate/ceramint

Structural and magnetic evaluation of substituted $NiZnFe_2O_4$ particles synthesized by conventional sol–gel method

Ali Ghasemi*, Mohammad Mousavinia

Department of Materials Engineering, Malek Ashtar University of Technology, Shahin Shahr, Iran

Received 31 July 2013; received in revised form 6 October 2013; accepted 10 October 2013
Available online 17 October 2013

Abstract

The aim of this study is to evaluate the structural and magnetic properties of Ni–Zn doped ferrite with trivalent Al^{3+} and Cr^{3+} cations substitution in $Ni_{0.6}Zn_{0.4}Fe_{2-x}Cr_{x/2}Al_{x/2}O_4$ ($x=0$, 0.1, 0.2, 0.3, 0.4 and 0.5) synthesized by employing conventional sol–gel method. X-ray diffraction (XRD), Fourier transform infrared (FTIR) spectroscopy, field emission scanning electron microscopy (FE-SEM), Mössbauer spectroscopy (MS) and vibrating sample magnetometer (VSM) analysis were carried out in order to characterize the structural and magnetic properties of particles. The XRD results confirmed the formation of single phase of spinel ferrite particles for a whole series of samples. The results of FTIR analysis indicated that the functional groups of Ni–Zn spinel ferrite were formed during the sol–gel process. Furthermore, FE-SEM micrographs revealed that the distribution of particles size is narrow. According to Mössbauer spectra,the doped cations are replaced in iron site occupancy of octahedral sites. It was found that with an increase in substitution contents magnetization decreased due to occupation of Al and Cr cations at low level substitutions in octahedral sites.

Keywords: C. Magnetic properties; Ni–Zn ferrite; Soft magnetic materials

1. Introduction

In case of magnetic ceramic materials, ferrites are exceptional magnetic materials widely used in microwave and electrical industries. They exhibit high electrical resistivity combined with useful ferromagnetic behavior [1]. There are several different synthesis methods used to fabricate ferrites as reported in literatures including sol–gel [2], coprecipitation [3], hydrothermal [4], mechano-chemical [5], refluxing [6], precursor [7], and auto-combustion [8] methods. The spinel ferrites belong to an important group of magnetic materials, because of their significant magnetic properties particularly in radio frequency region, physical flexibility, high electrical resistivity, mechanical hardness and chemical stability [9]. Among spinel ferrites, Ni–Zn ferrites are one of the most versatile soft magnetic materials. Recently, the synthesis process, characteristics and technological application of these materials have been studied extensively [10] due to their potential applications in many electronic devices owing to their high permeability at high frequency, remarkably high electrical resistivity, low eddy-current loss and reasonable cost [11–14]. The spinel structure of soft magnetic materials possesses the chemical formula of $(A)[B_2]O_4$, where A expresses the cations in tetrahedral sublattice sites and B represents the cations in octahedral positions in a cubic structure. However, in case of spinel ferrites the chemical formula $(A_{1-i}B_i)[A_iB_{2-i}]O_4$ represents many possible intermediary cation distributions that denote considerable cation disorder, indicating that spinel structure requires special attention in terms of magnetic characterization [15]. Spinel ferrites crystallize in the face-centered cubic (FCC) structure. The spinel crystal structures are usually categorized by inverse and normal structures. In the normal spinel structure A is a divalent element atom, occupying tetrahedral A sites, while B is a trivalent element sitting on the octahedral B sites. When A is a trivalent element which occupies tetrahedral site and B consists of equal numbers of trivalent and divalent elements, distributed over octahedral sites, the spinel structure is referred to as the inverse kind. The schematic picture of spinel structure is shown in Fig. 1. The Ni–Zn ferrite is a well-known mixed inverse spinel [16] whose unit cell is represented by the formula $(Zn_xFe_{1-x})[Ni_{1-x}\ Fe_{1+x}]O_4$ [17],

---

*Corresponding author. Tel./fax: +98 312 52 20731.
E-mail address: ali13912001@yahoo.com (A. Ghasemi).

0272-8842/$ - see front matter © 2013 Elsevier Ltd and Techna Group S.r.l. All rights reserved.
http://dx.doi.org/10.1016/j.ceramint.2013.10.031

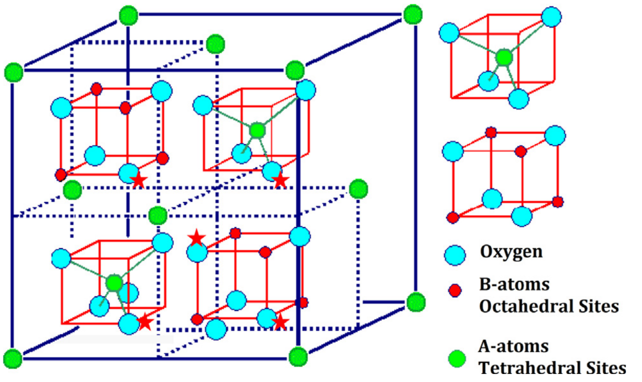

Fig. 1. Schematic picture of spinel structure; star means the intermediary cation sites that denote considerable cation disorder.

whereas the intrinsic magnetization (magnetic moment or total theoretical Bohr magneton of the lattice spinel) results from the inverse and normal phase, i.e., the distribution of cations in the spinel lattice. Based on these facts, the intrinsic magnetization of Ni–Zn ferrite can be calculated with and without the addition of 0.1 mol of chromium ions. Based on Hund's Rules [18], the magnetic moments of Fe^{3+}, Cr^{3+}, Al^{3+}, Ni^{2+} and Zn^{2+} are 5, 3, 0, 2 and $0\mu_B$, respectively. The addition of impurities induces changes in the defect structure and texture of the crystal [19], creating significant modifications in the magnetic and electrical properties of these materials. Several researchers have studied the effects of Cr^{3+} substitution in the spinel structure of ferrites [19–21]. However, the effect of Cr–Al cations simultaneously, has not been studied extensively yet.

In this research, the effect of Cr–Al cations simultaneous substitution was evaluated on the structural and magnetic properties of NiZn ferrite in order to correlate magnetic analysis and reflection loss characteristic in MHz band for near future literatures in the field. With this view in mind, the present paper is intended to clarify the characteristic magnetic properties of this ferrite. For obtaining this goal, the prepared samples were characterized using X-ray diffraction (XRD), Fourier transformed spectroscopy (FTIR), field emission scanning electron microscopy (FE-SEM), Mössbauer spectroscopy (MS), and vibrating sample magnetometer (VSM).

2. Experimental

2.1. Synthesis process

The Cr–Al doped ferrite $Ni_{0.6}Zn_{0.4}Fe_{2-x}Cr_{x/2}Al_{x/2}O_4$ with x=0, 0.1, 0.2, 0.3, 0.4, and 0.5 powders was synthesized by use of conventional sol–gel method. Consequently, the stoichiometric amounts of precursors including citric acid ($C_6H_8O_7$), $Fe(NO_3)_3\cdot 9H_2O$, $Ni(NO_3)_2\cdot 6H_2O$, $Zn(NO_3)_2\cdot 4H_2O$, $Cr(NO_3)_3\cdot 9H_2O$, and $Al(NO_3)_3\cdot 9H_2O$ were employed to synthesize the soft magnetic powders. At first, an amount of citric acid was dissolved in distilled water. Citric acid helps in the homogenous distribution and segregation of metal ions. The metal nitrates were added to the solution. The solution was circulated and heated using magnetic stirrer at a temperature of 80 °C. The viscous gel was obtained after evaporation of water from solution and the occurring polymerization reactions during sol–gel process. Consequently, the dried gel was placed in an oven at a temperature of 200 °C. Finally, the powders were calcined at a temperature of 1300 °C for 3 h.

2.2. Measurements

X-ray diffraction measurements (XRD) were performed for phase evaluation of the synthesized samples using a Philips diffractometer (MPD-XPET model) with Cu k_α radiation operated at 40 kV and 30 mA. FTIR spectroscopy was carried out to evaluate the functional groups which were formed during sol–gel process using a 680PLUS JESCO spectrometer. In order to evaluate the microstructure of the powders, FE-SEM micrographs were taken using a JEOL scanning electron microscope with an accelerating voltage of 15 kV. ^{57}Fe Mössbauer spectroscopic measurements were performed in transmission geometry at 293 K. ^{57}Co/Rh was used as gamma ray and quantitative investigations were carried out using software. A vibrating sample magnetometer was used to measure the magnetic properties of the calcined ferrite powders at ambient temperature. The magnetic hysteresis loops were measured at room temperature with maximum applied magnetic field of 10 kOe. The magnetic field sweep rate was 5 Oe/s for all measurements.

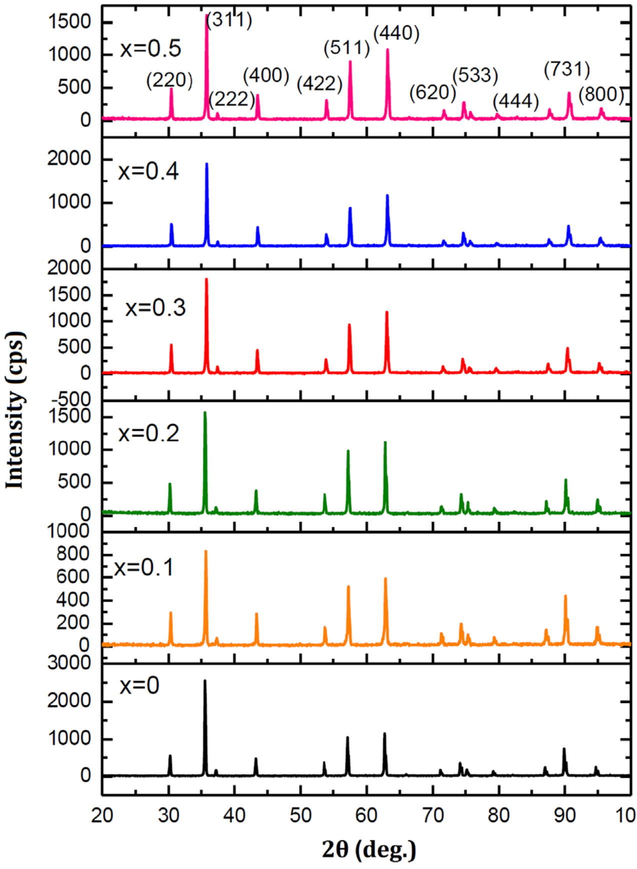

Fig. 2. X-ray diffraction (XRD) patterns of the synthesized powders.

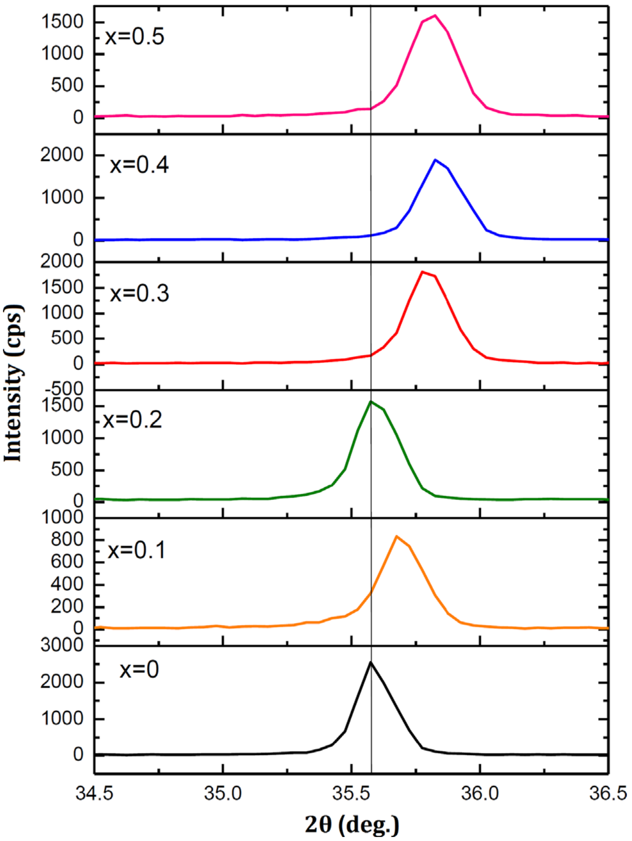

Fig. 3. Shift in position of (311) diffraction peak with increasing doping.

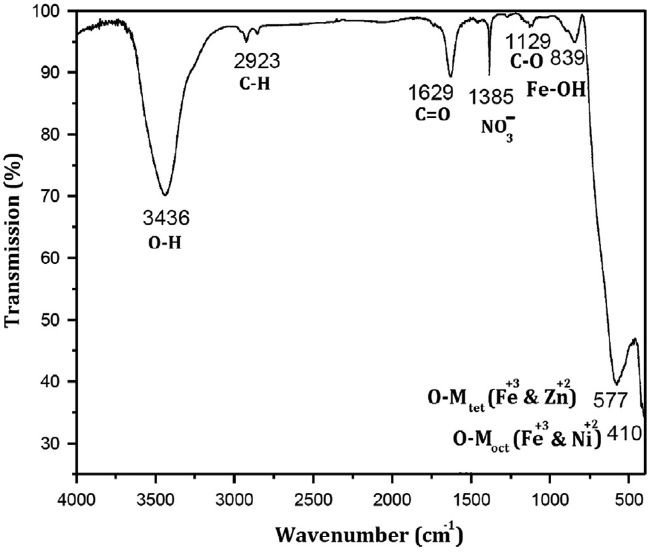

Fig. 4. FTIR spectra of the pure NiZn sample (x=0).

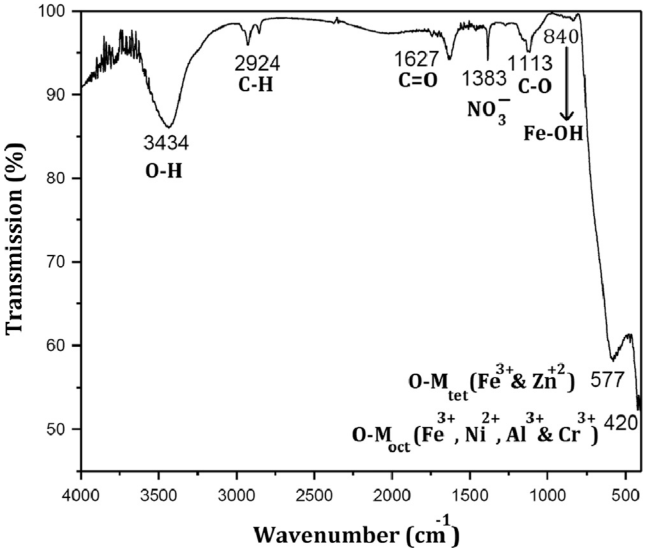

Fig. 5. FTIR spectra of the Al–Cr doped NiZn sample (x=0.1).

3. Results and discussion

3.1. Structural properties

3.1.1. XRD analysis

Phase evaluation of all synthesized samples was carried out using X-ray diffraction (XRD) technique. The XRD patterns of $Ni_{0.6}Zn_{0.4}Fe_{2-x}Cr_{x/2}Al_{x/2}O_4$ spinel ferrite compound with x=0–0.5 in step of 0.1 are shown in Fig. 2. A close examination of the pattern reveals the presence of well defined, sharp and intense peaks which confirms that the Cr–Al doped NiZn ferrite samples have crystallized well. The NiZn ferrite phase were characterized by the (311), (511), and (440) diffraction peaks in 35.6, 57.11, and 62.7 diffraction angles, respectively. The miller indices of each appeared peak in the structure was determined in XRD patterns. The diffraction peaks confirm the formation of single phase cubic spinel structure for all samples without any impurity or secondary phase. All of the characterized peaks are marked with the standard of the American Society for Testing and Materials (JCPDS card no. 019-0629). Furthermore, the diffraction angles of peaks corresponding to the doped NiZn ferrite appeared at almost a different position from the undoped NiZn ferrite peaks, and another difference being the peak intensity. This appeared phenomenon is shown in Fig. 3. The shift in the position of the doped NiZn ferrite peaks is related to the substitution of chromium and aluminum cations in the cubic crystal structure of the substituted NiZn ferrite. The ionic radius of Cr, Al, and Fe cations are 0.64, 0.53, and 0.67 Å, respectively. The substitution of Cr and Al with smaller ionic radii compared to the Fe cations leads to shrinkage of the cubic crystal structure of spinel phase. In fact, the replacement of Fe cations by Cr and Al cations the crystal lattice constant and consequently the distance between crystal planes decreased, and according to the Bragg equation the diffraction angle increases. The relation between crystal plain distance in cubic crystal lattice and lattice parameter and also Bragg equation are explained below:

$$a = d_{hkl}\sqrt{(h^2+k^2+l^2)} \qquad (1)$$

$$n\lambda = 2d\ \sin\ \theta \qquad (2)$$

In these equations a is lattice parameter, d is the distance between lattice planes, (h, k, l) is miller indices, n is an integer,

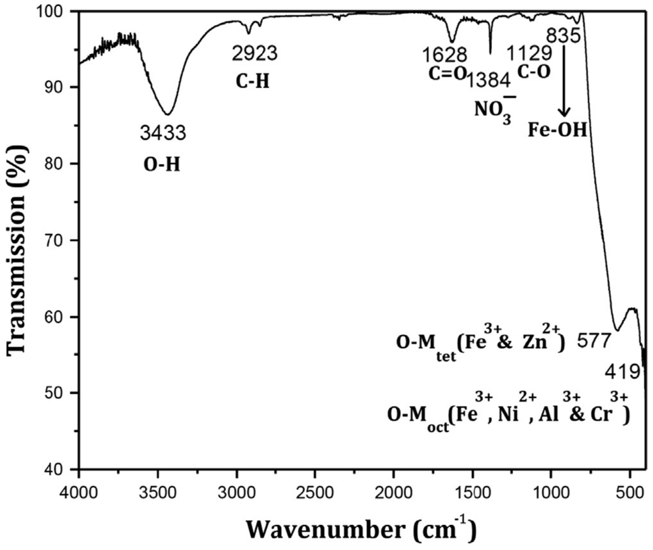

Fig. 6. FTIR spectra of the Al–Cr doped NiZn sample ($x=0.2$).

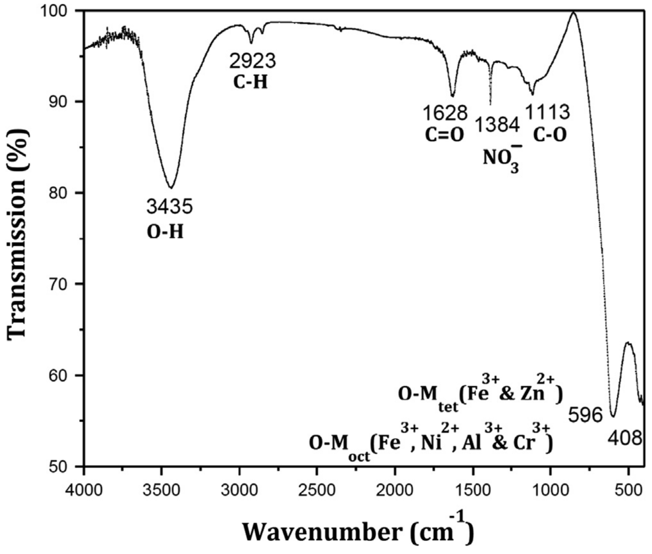

Fig. 8. FTIR spectra of the Al–Cr doped NiZn sample ($x=0.4$).

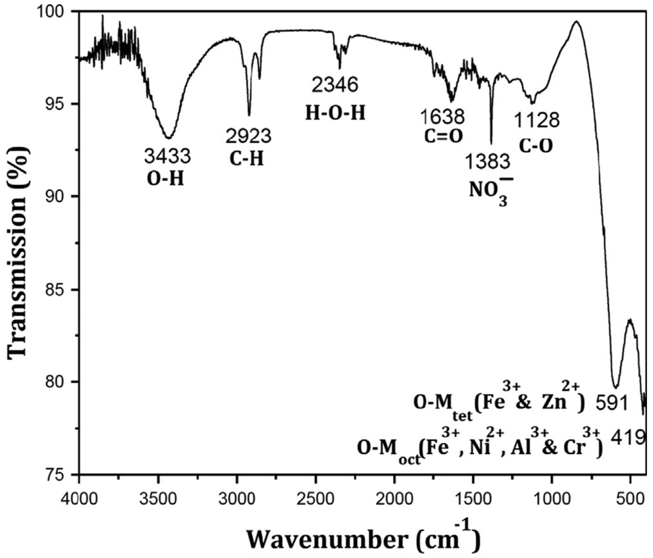

Fig. 7. FTIR spectra of the Al–Cr doped NiZn sample ($x=0.3$).

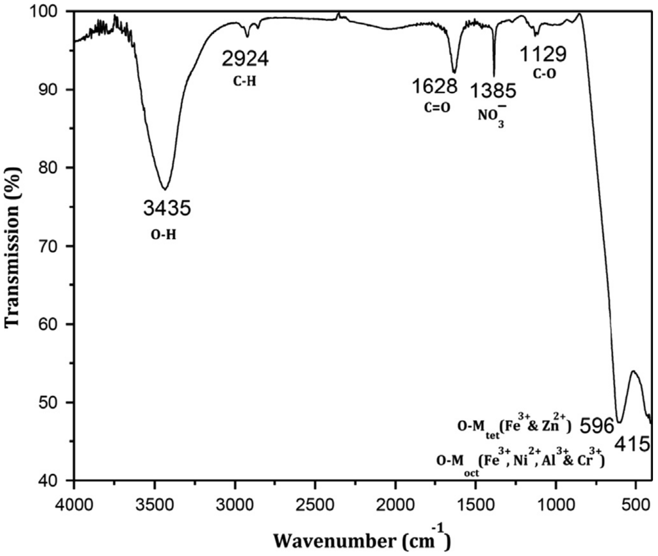

Fig. 9. FTIR spectra of the Al–Cr doped NiZn sample ($x=0.5$).

λ is the wavelength of X-ray, and θ is diffraction angle. The crystallite size can be measured by the Scherer equation which is expressed as

$$D=k\lambda/\beta \cos\theta \tag{3}$$

where D is crystallite size, k is a dimensionless shape factor, with a value close to unity. The shape factor has a typical value of about 0.9, but varies with the actual shape of the crystallite, λ is the X-ray wavelength in nanometer (nm), β is the (311) peak width of the diffraction peak profile at half maximum height resulting from small crystallite size in radians, and θ is diffraction angle. The value of 2β axis of diffraction profile must be in radians. The θ can be in degrees or radians, since the $\cos\theta$ corresponds to the same number. It can be taken as 0.89 or 0.9 for full width half maximum (FWHM) of spherical crystals with cubic unit cells. For an excellent discussion of K, it is better to refer to Ref. [22]. By increasing the substitution content the crystallite size decreased from 50 nm to 38 nm which results in promotion of porosity. In fact, with a decrease in crystallite size, the crystallite boundaries and the surface area between the crystallites will be increased which leads to increase in porosity content in powders.

3.1.2. FTIR analysis

The FTIR spectra of $Ni_{0.6}Zn_{0.4}Fe_{2-x}Cr_{x/2}Al_{x/2}O_4$ ($x=0$–0.5) as-prepared samples are shown in Figs. 4–9. The variation in bonds vibration is due to the difference in distance between ions in both octahedral and tetrahedral sublattice sites. There

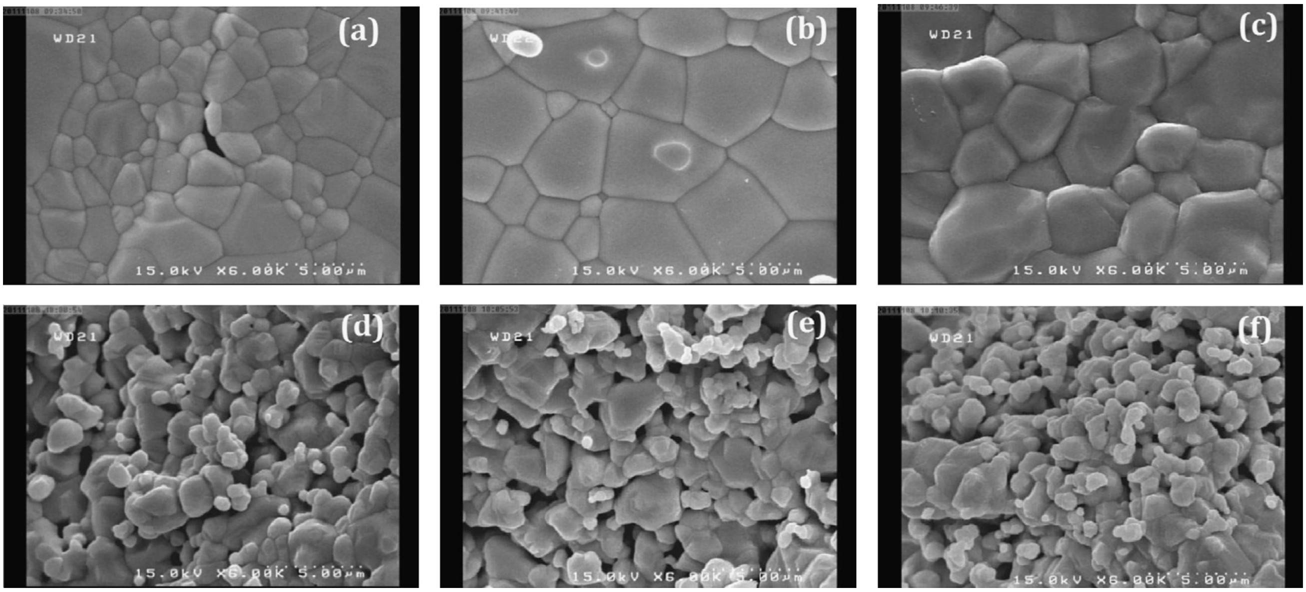

Fig. 10. FE-SEM micrographs of Al–Cr doped NiZn sample, (a) $x=0$, (b) $x=0.1$. (c) $x=0.2$, (d) $x=0.3$, (e) $x=0.4$, and (f) $x=0.5$.

are two bonds within the range of 400–600 cm^{-1} which are the characteristic bonds of the spinel structure. The high frequency bond (577 cm^{-1}, 591 cm^{-1}, and 596 cm^{-1}) and the low frequency bond (408 cm^{-1}, 410 cm^{-1}, 415 cm^{-1}, 419 cm^{-1}, and 420 cm^{-1}) are in accordance with the vibration of Fe^{3+}–O^{2-} complexes vibrations in octahedral and tetrahedral sites, respectively. The vibration of functional groups in tetrahedral sites occurs at higher frequencies than those for octahedral sites, which is due to the smaller bond length of tetrahedral positions compared to the octahedral sites. The reduction of lattice parameter due to the doping of chromium and aluminum cations influence the stretch vibration of Fe^{3+}–O^{2-} complexes and consequently plays the main role in deviation of bonds positions [23,24]. According to the information derived by some researchers [25–28], it is known that Ni^{2+}, Cr^{3+}, and Al^{3+} cations have octahedral-site preference, whereas in an inverse-spinel Cr–Al doped NiZn ferrite, Zn^{2+} prefers the tetrahedral site. Moreover, Fe^{3+} cations can occupy both octahedral and tetrahedral sites. The peaks with wavenumber of 835 cm^{-1}, 839 cm^{-1}, and 840 cm^{-1} in Figs. 4–6 are due to the vibration of Fe–OH bond. The peaks with wavenumber of 1113 cm^{-1}, 1128 cm^{-1}, and 1129 cm^{-1} are due to stretch vibration of C–O bond. The peaks with wavenumber of 1383 cm^{-1}, 1384 cm^{-1}, and 1385 cm^{-1} are due to stretching vibration of nitrate (NO_3^-) groups, indicating that nitrate ions are present in the calcined samples. The peaks appearing around 1627 cm^{-1}, 1628 cm^{-1}, 1629 cm^{-1}, and 1638 cm^{-1} are due to asymmetric stretching of carbonyl groups (C=O). The peak appearing around 2346 cm^{-1} is due to the bending vibration of H–O–H bond of absorbed water. The peaks appearing around 2923 cm^{-1}, and 2924 cm^{-1} are due to stretching vibration of C=H bond of CH_3 functional group. The peaks at 3433 cm^{-1}, 3434 cm^{-1}, 3435 cm^{-1}, and 3435 cm^{-1} are due to stretching vibration of O–H bonds of water and the broad nature of these peaks is related to the presence of hydrogen-bonded chains [29–31].

3.1.3. FE-SEM analysis

The FE-SEM micrographs of the $Ni_{0.6}Zn_{0.4}Fe_{2-x}Cr_{x/2}Al_{x/2}O_4$ (x=0–0.5) powders calcined at 1300 °C for 3 h, are shown in Fig. 10. As, can be seen, the microstructure of the synthesized powders including, morphology, particle size and porosity is influenced by doping of Cr–Al cations in the spinel structure. By using Microstructural Image Processing software (MIP 4.1 full; Nahamin Pardazan Asia, I.R. Iran), it is concluded that the estimated average particle sizes are approximately within the range of 1–4 μm for samples ($x=0$), ($x=0.1$), and ($x=0.2$). The growth of particle size is due to performing high calcining temperature of the synthesizing process. Additionally, the loss of the fine particle nature of ferrites by the conventional method is due to the high heating temperatures involved. As a matter of fact, substitution of Cr–Al doped cations has no main effect in change of particle size. Consequently, by increasing the Cr–Al substitution value in the structure, the particle size, morphology, and also, porosity content were influenced. Addition of Cr and Al cations in high level substitution $x=0.3$–0.5 results in reduction of particle size effectively from 2 μm to 500 nm. The doped cations decrease the growth rate of particles and consequently the particle size is decreased by substitution. The porosity formed between the particles, increased by increasing of substitution value which is due to the smaller ionic size of the Cr–Al doped cations. As explained in Section 3.1.1., the displacement of Fe cations by Cr and Al cations leads to shrinkage of the crystal lattice, decrease in crystallite size and consequently increase in crystallite boundaries. Moreover, the total density of the lattice is decreased due to smaller density of the doped cations compared to Fe cations which directly influence the porosity content of the powders. The Cr–Al doped NiZn ferrite particles prepared by the

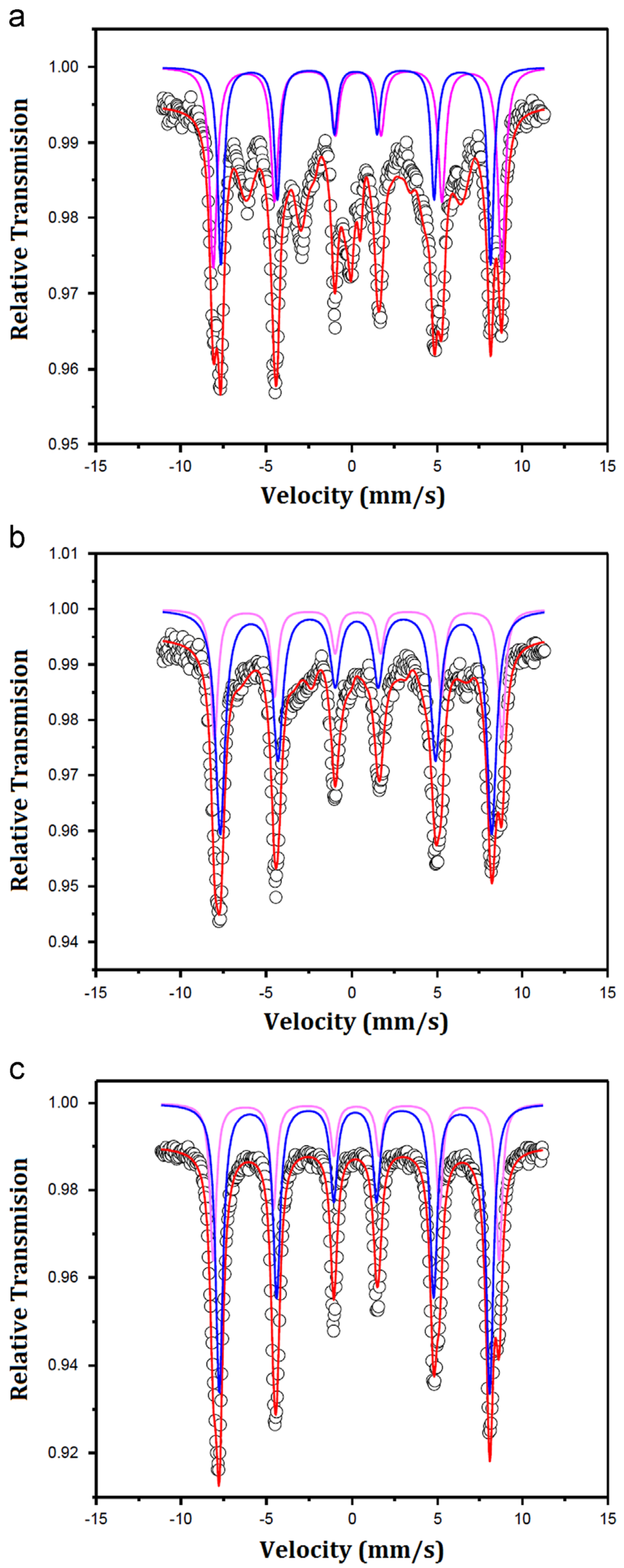

Fig. 11. Mössbauer spectra of $Ni_{0.6}Zn_{0.4}Fe_{2-x}Cr_{x/2}Al_{x/2}O_4$ ($x=0$, 0.3, and 0.5) ferrite particles.

conventional sol–gel method being almost large in size, a tendency towards agglomeration is observed. The magneto–dipole interactions between the particles may cause the agglomeration of the particle with increasing substitution content [32].

3.1.4. Mössbauer studies

Mössbauer spectra of $Ni_{0.6}Zn_{0.4}Fe_{2-x}Cr_{x/2}Al_{x/2}O_4$ ($x=0$, 0.3, and 0.5) ferrite particles is shown in Fig. 11. ^{57}Fe Mössbauer spectroscopic measurements were performed in transmission geometry using a $^{57}Co/Rh$ γ-ray source. High-field Mössbauer measurements were carried out at 298 K in an external magnetic field of 51.4 T applied parallel to the γ-ray direction. The velocity scale calibrated relative to ^{57}Fe in Rh. Recoil spectral analysis software [33] was used for the quantitative evaluation of the Mössbauer spectra. The Mössbauer parameters including isomer shift (δ), quadrupole splitting (QS), outermost linewidth (Γ), hyperfine magnetic field (B_{hf}), and fractional area of each subspectrum (A), are given in Table 1. Using peak intensities and fractional area of each subspectrum, the Fe^{3+} ion ratio in both octahedral and tetrahedral sublattice sites was calculated. According to the Mössbauer parameters, the fractional area of tetrahedral sites was decreased from 27.1 for undoped sample ($x=0$) to 23.2, and 20.5 for ($x=0.3$) and ($x=0.5$) samples, respectively. Consequently, the fractional areas of octahedral sites were increased from 23.2 for undoped sample ($x=0$) to 28.4, and 32.1 for ($x=0.3$) and ($x=0.5$) samples, respectively. This site preference occupancy confirmed the reduction of Fe^{3+} cations in octahedral sites and it is concluded that the Cr^{3+} and Al^{3+} cations preferred to occupy the octahedral sites. The chromium and aluminum elements are categorized in paramagnetic state and have down-spin configuration, in spite of the fact that Fe^{3+} cations have ferromagnetic characteristics, and also have up-spin configuration. However, the substitution of ferromagnetic Fe^{3+} cations by paramagnetic Cr^{3+} and Al^{3+} cations result in a reduction of total magnetic moment, and consequently the magnetization in octahedral sites was decreased. The distribution of Fe^{3+} ions amongst the A and B sublattices can be realized from the relation between the area ratio of B to A site subspectra and stoichiometric value x as illustrated in Table 2. The decrease of this ratio against x clears that the substitution process often reduces the Fe^{3+} number in the lattice at the expense of the number of Fe^{3+} ions at the sublattice. It is well known that the Zn^{2+} ions exclusively occupy the A-sites, the Cr^{3+} and Al^{3+} ions the B-sites and the preferred site for the Ni^{2+} ions is the B-sites. Consequently the cation distribution can be estimated, as given in Table 2, using the site preference of elements and the ratio of area under the well resolved subspectra belonging to the A and B sublattices. The behavior of hyperfine magnetic field at octahedral and tetrahedral sites showed that, with increase of Cr^{3+} and Al^{3+} cations, this parameter decreased. This can be inferred on the basis of decreasing the magnetic superexchange interaction between and within the sublattices due to the reduction of Fe^{3+} cations number. It is necessary to consider not only the tetrahedral–octahedral (A–B) superexchange but also the octahedral–octahedral (B–B) supertransferred hyperfine interactions [34]. In the cation distribution, Cr^{3+} and Al^{3+} ions are non-magnetic and do not contribute to the

Table 1
Lattice parameters and crystallite size of the samples.

Samples	$x=0$	$x=0.1$	$x=0.2$	$x=0.3$	$x=0.4$	$x=0.5$
Lattice parameter (a) (Å)	8.353	8.341	8.334	8.328	8.326	8.313
Crystallite size (nm)	50	41	41	41	41	38

Table 2
Mössbauer parameters of samples where δ, QS, Γ, B_{hf}, and A are the isomer shift, quadrupole shift (or the quadrupole doublet splitting), hyperfine magnetic field, outermost linewidth and fractional area of each (site) subspectrum, respectively.

Samples	Sitio	δ (mm/s)	QS (mm/s)	δ (mm/s)	B_{hf} (T)	A (%)
$Ni_{0.6}Zn_{0.4}Fe_2O_4$	Sextet 1(tetrahedral site)	0.36	−0.01	0.52	51.4	27.1
	Sextet 2 (octahedral site)	0.24	+0.01	0.41	49.2	23.2
$Ni_{0.6}Zn_{0.4}Fe_{1.7}Cr_{0.15}Al_{0.15}O_4$	Sextet 1(tetrahedral site)	0.35	−0.02	0.48	50.1	23.2
	Sextet 2 (octahedral site)	0.28	+0.04	0.51	48.3	28.4
$Ni_{0.6}Zn_{0.4}Fe_{1.7}Cr_{0.25}Al_{0.25}O_4$	Sextet 1(tetrahedral site)	0.34	−0.03	0.47	49.1	20.5
	Sextet 2 (octahedral site)	0.31	+0.05	0.53	50.2	32.1

nuclear magnetic field. Also, the Fe^{3+}–O^{2-}–Fe^{3+} superexchange interaction is higher than the Fe^{3+}–O^{2-}–Cr^{3+}, Cr^{3+}–O^{2-}–Fe^{3+}, Fe^{3+}–O^{2-}–Al^{3+}, and Al^{3+}–O^{2-}–Fe^{3+} [35]. As a result, B_{hfA} and B_{hfB} decrease with increasing Cr^{3+} and Al^{3+} content instead of Fe^{3+} ions and lead to decreasing the number of the magnetic bonds Fe_A^{3+}–O^{2-}–Fe_B^{3+}. Increasing B_{hfB}, for $x=0.5$ may be attributed, in addition to the magnetic superexchange interactions within the sublattice, to the supertransferred A–A and B–B magnetic hyperfine interactions between the magnetic Fe^{3+}, Cr^{3+} and Al^{3+} ions entering the A and B sublattices. It may arise from a ferromagnetic interaction between the Fe^{3+} and Ni^{2+} magnetic ions within the sublattice. The outermost line width (Γ) of the B magnetic sites increases with x, whereas that of the A magnetic sites decreases with increasing substitution as shown in Table 2. This may be attributed to the change of the Fe^{3+} ions at the A and B site. The linewidth of the ^{57}Fe Mössbauer spectra is useful for estimating the influence of cation disorder on both electric and magnetic interactions. It has been shown that the widths of the outermost lines are about six times more sensitive than those of the innermost lines to fluctuation effects in the magnitudes of the hyperfine field, whereas the widths of all the lines are equally sensitive to variations in the quadrupole coupling constant [36]. The isomer shift values (δ) for Fe^{3+} ions at the A-sites and B-sites (Table 2), lie between 0.36–0.34 mm/s and 0.24–0.31 mm/s, respectively, which is consistent with high-spin Fe^{3+} charge states [37]. With increasing substitution of Cr–Al cations in octahedral sites, the isomer shift parameter increases from 0.24 mm/s to 0.31 mm/s while there is a decrease from 0.36 mm/s to 0.34 mm/s for octahedral and tetrahedral sites, respectively. Such behavior of IS (A) and IS (B) is expected due to differences in the Fe^{3+}–O^{2-} internuclear separations. The absolute quadrupole shift values increase from 0.01 mm/s to 0.05 mm/s while there is a decrease from −0.01 mm/s to −0.03 mm/s for octahedral and tetrahedral sites, respectively. Generally, the high value of quadrupole splitting is related to chemical disorder of the samples, i. e. existing cations of different charges and radii in the sublattices. However, the relatively same values of QS_A and QS_B may be due to the presence of small electric field gradient (EFG) acting on iron nuclei corresponding to Fe^{3+} ions in octahedral and tetrahedral sites.

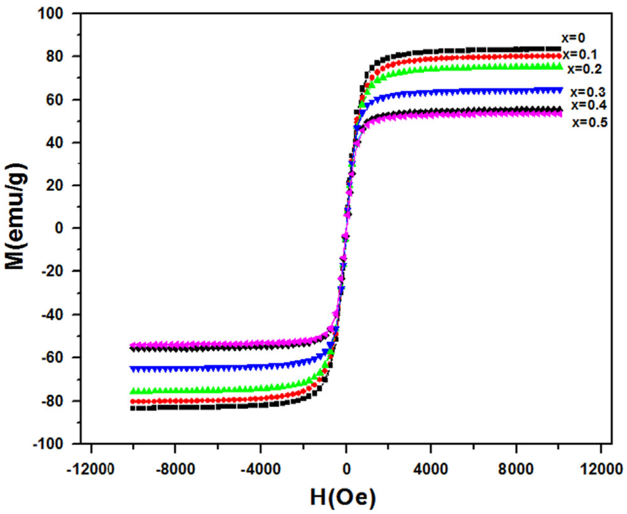

Fig. 12. Hysteresis loops of $Ni_{0.6}Zn_{0.4}Fe_{2-x}Cr_{x/2}Al_{x/2}O_4$ ferrite particles.

3.2. Magnetic properties

3.2.1. VSM analysis

Substitution of Cr^{3+} and Al^{3+} ions instead of Fe^{3+} cations significantly influenced the magnetic characteristic of NiZn ferrite. The magnetic hysteresis loops of undoped and substituted NiZn ferrite are shown in Fig. 12. This figure indicates that NiZn ferrite is a soft magnetic material with minimal hysteresis. The large saturation magnetization and small

Table 3
Magnetic parameters of $Ni_{0.6}Zn_{0.4}Fe_{2-x}Cr_{x/2}Al_{x/2}O_4$ ($x=0$–0.5) ferrite particles.

Samples	$x=0$	$x=0.1$	$x=0.2$	$x=0.3$	$x=0.4$	$x=0.5$
Saturation magnetization (M_s) (emu/g)	83.4	81.6	75.2	64.5	55.1	53.6
Coercivity (H_c) (Oe)	12.6	14.7	15.8	19.5	21.1	24.7

coercivity of the Ni–Zn ferrite sample can be ascribed to the high crystallinity and uniform morphologies [38]. The hysteresis loops of the particles synthesized at 1300 °C expressed the ferrimagnetic behavior which is due to large magnetic particle size with large amount of ordered spins. The obtained results reveal that the saturation magnetization of the as-prepared ferrites, M_s, decreased, while the coercivity, H_c, raised with increasing substitution value, x. The magnetic parameters of samples are given in Table 3. In spinel crystal structure of Cr–Al-doped NiZn ferrite, Ni^{2+} cations have octahedral site preference, Zn^{2+} cations prefer to occupy the tetrahedral sites, and Fe^{3+} can occupy the both octahedral and tetrahedral sites. It is worthy to note that, the total magnetization of the lattice originates from the difference between the magnetization of octahedral and tetrahedral sites, which can be described as $M=|M_b-M_a|$ The magnetic moment in ferrite is mainly due to the uncompensated electron spin of the individual ions and the spin alignments in the two sublattices, which are arranged in an antiparallel mode. In a spinel ferrite, each ion at the A site has 12 B-site ions as the nearest neighbors. According to Neel's molecular-field model [39], the A–B superexchange interaction predominates the intrasublattice A–A and B–B interactions. Therefore, the net magnetic moment is given by the sum of the magnetic moments of the A and B sublattices. In case of Cr–Al-substituted Ni–Zn ferrite, the Fe^{3+} cations are replaced by Cr^{3+} and Al^{3+} ions, leading to a decrease in the B-site sublattice magnetization. Therefore, the magnetization of the B sublattices decreases, which leads to a decrease in the net magnetization. The decrease in magneton number is explained by the A–B interaction. In the present case, Cr^{3+} and Al^{3+} ions with low magnetic moment values, ($3\mu_B$) and near zero, respectively, replace Fe^{3+} ions of high magnetic moment ($5\mu_B$). According to the cation distribution data from Mössbauer spectra, Cr^{3+} and Al^{3+} ions occupy octahedral B sites. This placement leads to a decrease of the magnetic moment of the B site, and therefore the Bohr magneton number decreases with substitution. The magnetization is a function of the number of directed spins per unit volume. Thus, the decreasing of the saturation magnetization with increasing content of doped cations is caused by a reduction in the number of directed spins per unit volume. Furthermore, the decrease in saturation magnetization may be attributed to the hard reversible displacement or domain wall movement in the direction of the applied magnetic field. For this displacement to occur, the energy of the domain wall pinning must be greater than that of the applied external field. Thus, the harder the displacement, the smaller the saturation magnetization [40]. It is well known that the coercivity is highly dependent on major parameters such as the particle size and anisotropy constant. By decreasing particle size, the coercivity typically increases [41]. The coercivity for uniaxial system and submicron particles is expressed by

$$H_c = 2K_1/\mu_o M_s \tag{4}$$

In this equation, K_1 is the first anisotropy constant, μ_o is permeability of free space, M_s is the saturation magnetization, and H_c is the coercivity. The coercivity can be altered by heat treatment or deformation and thus is independent of saturation magnetization. Regarding the FE-SEM micrographs, the particle size is decreased by increasing substitution and consequently influences coercivity. In other words, a decrease in particle size results in an increase in coercivity. Experimental investigation of the dependence of coercivity on particle size showed that the coercivity H_c increases with decreasing grain size D down to values of about 40 nm, independent of the kind of material. The increase of H_c is proportional to $1/D$. The reason for this is that in small particles the formation of a closed magnetic flux becomes energetically less favorable so that the magnetic domain size with a uniform magnetization becomes more and more identical with the grain size. This grain size is defined as the first critical size (D_c, which is characteristic of each material) where the multidomain materials change to a monodomain material. This leads to a strong increase of the coercivity (or high remanence) because a change of magnetization in this case cannot happen only by shifting the domain walls which normally requires only a weak magnetic field [42]. Similarly, microstructural defects such as porosity greatly influence the coercivity. According to FE-SEM micrographs, the porosity content of the powders was increased with increasing substitution. Porosity affects the magnetization process because the pores work as a generator of a demagnetizing field. As the porosity increases, a higher field is needed to push the domain wall, increasing H_c. The saturation magnetization is related to H_c through Brown's relation [43]. According to this relation, H_c is inversely proportional to M_s, which is consistent with the obtained experimental results. Thus, the smaller the saturation magnetization, the larger the coercivity.

4. Conclusions

The Cr–Al doped NiZn ferrite $Ni_{0.6}Zn_{0.4}Fe_{2-x}Cr_{x/2}Al_{x/2}O_4$ ($x=0$–0.5) particles were synthesized using conventional sol–gel process. The XRD results confirm the formation of single-phase cubic spinel structure for all the samples. The diffraction angle of the nanoparticles shifted to higher degrees due to a decrease in lattice constant with increasing substitution. According to FTIR analysis, there are two peaks in the range of 400–600 cm^{-1} which are the characteristic bonds of the spinel structure. The low frequency bonds, typically observed in the range of 450–400 cm^{-1}, are assigned to the metal–oxygen stretching at octahedral site, $M_{octa} \leftrightarrow O$. These characteristic bonds revealed the replacement of Cr–Al doped cations instead of Fe cations in the crystal structure. The FE-SEM micrographs revealed the formation of particles with 500 nm to 4 μm in size. The as-prepared Cr–Al doped NiZn ferrite particles being almost large in size, a tendency towards agglomeration is observed. According to Mössbauer spectra, the Cr–Al doped cations prefer to occupy the octahedral sites. The hysteresis curves of the particles exhibited the reduction of saturation magnetization with an increase in substitution value, which is due to substitution of paramagnetic cations in octahedral sublattices. The magnetic characteristics represented the ferrimagnetic behavior among the particles.

References

[1] C. Venkataraju, G. Sathishkumar, K. Sivakumar, Effect of cation distribution on the structural and magnetic properties of nickel substituted nanosized Mn–Zn ferrites prepared by co-precipitation method, J. Magn. Magn. Mater. 322 (2010) 230–233.

[2] A. Pradeep, P. Priyadharsini, G. Chandrasekaran, Sol–gel route of synthesis of nanoparticles of $MgFe_2O_4$ and XRD, FTIR and VSM study, J. Magn. Magn. Mater. 320 (2008) 2774–2779.

[3] S.G. Doh, E.B. Kim, B.H. Lee, J.H. Oh, Characteristics and synthesis of Cu–Ni ferrite nanopowders by coprecipitation method with ultrasound irradiation, J. Magn. Magn. Mater. 272–276 (2004) 2238–2240.

[4] B. Baruwati, R.K. Rana, S.V. Manorama, Further insights in the conductivity behavior of nanocrystalline $NiFe_2O_4$, J. Appl. Phys. 101 (2007) 014302–014308.

[5] H. Yang, X. Zhang, W. Ao, G. Qiu, Formation of $NiFe_2O_4$ nanoparticles by mechanochemical reaction, Mater. Res. Bull. 39 (2004) 833–837.

[6] X.D. Li, W.S. Yang, F. Li, D.G. Evans, X. Duan, Stoichiometric synthesis of pure $NiFe_2O_4$ spinel from layered double hydroxide precursors for use as the anode material in lithium-ion batteries, J. Phys. Chem. Solids 67 (2006) 1286–1290.

[7] M.M. Hessien, Synthesis and characterization of lithium ferrite by oxalate precursor route, J. Magn. Magn. Mater. 320 (2004) 2800–2807.

[8] L. Ai, J. Jiang, Influence of annealing temperature on the formation, microstructure and magnetic properties of spinel nanocrystalline cobalt ferrites, Curr. Appl. Phys. 10 (2010) 284–288.

[9] M. Tan, Y. Köseoğlu, F. Alan, E. Şentürk, Overlapping large polaron tunneling conductivity and giant dielectric constant in $Ni_{0.5}Zn_{0.5}Fe_{1.5}Cr_{0.5}O_4$ nanoparticles (NPs), J. Alloys Compd. 509 (2011) 9399–9405.

[10] B.V. Bhise, M.B. Dongare, S.A. Patil, S.R. Sawant, X-ray infrared and magnetization studies on Mn substituted Ni–Zn ferrites, J. Mater. Sci. Lett. 10 (1991) 922–924.

[11] S.M. Patange, Sagar E. Shirsath, G.S. Jangam, K.S. Lohar, Santosh S. Jadhav, K.M. Jadhav, Rietveld structure refinement, cation distribution and magnetic properties of Al^{3+} substituted $NiFe_2O_4$ nanoparticles, J. Appl. Phys. 109 (2011) 053909–053917.

[12] S.M. Patange, Sagar E. Shirsath, B.G. Toksha, Santosh S. Jadhav, S. J. Shukla, K.M. Jadhav, Cation distribution by Rietveld, spectral and magnetic studies of chromium-substituted nickel ferrites, Appl. Phys. A 95 (2009) 429–434.

[13] S.M. Patange, Sagar E. Shirsath, K.S. Lohar, S.S. Jadhav, Nilesh Kulkarni, K.M. Jadhav, Electrical and switching properties of $NiAl_xFe_{2-x}O_4$ ferrites synthesized by chemical method, Phys. B: Condens. Matter 406 (2011) 663–668.

[14] M.A. Ahmed, E. Ateia, L.M. Salah, A.A. El-Gamal, Structural and electrical studies on La^{3+} substituted Ni–Zn ferrites, Mater. Chem. Phys. 92 (2005) 310–321.

[15] P.N. Lisboa-Filho, C. Vila, G. Petrucelli, C.O. Paiva-Santos, L. Gama, W.A. Ortiz, E. Longo, Magnetic doping in $Zn_{7-x}M_xSb_2O_{12}$ spinels (M = Ni and Co), Physica B 320 (2002) 249–252.

[16] R.C. O'Handley, Modern Magnetic Materials—Principles and Applications, Wiley, USA, 2000.

[17] A.S. Albuquerque, J. Ardisson, W.A.A. Macedo, Propriedades magnéticas de ferrita de níquel e zinco, An. Congr. Bras. Ceram. 41 (1997) 142–145.

[18] S.M. Rezende, A Fisica de Materiais e Dispositivos Eletronicos, Editora da Universidade Federal de Pernambuco, Recife, 1996, pp. 392.

[19] A.M. El-Sayed, Electrical conductivity of nickel–zinc and Cr substituted nickel–zinc ferrites, Mater. Chem. Phys. 82 (2003) 583–587.

[20] S.M. Patange, S.E. Shirsath, B.G. Toksha, S.S. Jadhav, K.M. Jadhav, Electrical and magnetic properties of Cr^{3+} substituted nanocrystalline nickel ferrite, J. Appl. Phys. 106 (2009) 023914–023920.

[21] D.R. Mane, Swati Patil, D.D. Birajdar, A.B. Kadam, S.E. Shirsath, R. H. Kadam, Sol–gel synthesis of Cr^{3+} substituted $Li_{0.5}Fe_{2.5}O_4$: cation distribution, structural and magnetic properties, Mater. Chem. Phys. 126 (2011) 755–760.

[22] J. Langford, A. Wilson, Scherrer after sixty years: a survey and some new results in the determination of crystallite size, J. Appl. Crystallogr. 11 (1978) 102–103.

[23] S.E. Shirsath, B.G. Toksha, R.H. Kadam, S.M. Patange, D.R. Mane, G. S. Jangam, A. Ghasemi, Doping effect of Mn^{2+} on the magnetic behavior in Ni–Zn ferrite nanoparticles prepared by sol–gel autocombustion, J. Phys. Chem. Solids 71 (2010) 1669–1675.

[24] N. Singh, A. Agarwal, S. Sanghi, P. Singh, Effect of magnesium substitution on dielectric and magnetic properties of Ni–Zn ferrite, Physica B 406 (2011) 687–692.

[25] A.T. Raghavender, N. Biliškov, Ž. Skoko, XRD and IR analysis of nanocrystalline Ni–Zn ferrite synthesized by the sol–gel method, Mater. Lett. 65 (2011) 677–680.

[26] M. Tana, Y. Köseoğlu, F. Alan, E. Şentürk, Overlapping large polaron tunneling conductivity and giant dielectric constant in $Ni_{0.5}Zn_{0.5}Fe_{1.5}Cr_{0.5}O_4$ nanoparticles (NPs), J. Alloys Compd. 509 (2011) 9399–9405.

[27] J. Smith, H.P.J. Wijn, Ferrites, Wiley, New York, 1959.

[28] A.A. Sattar, H.M. El-Sayed, K.M. El-Shokrofy, M.M. El-Tabey, Effect of manganese substitution on the magnetic properties of nickel–zinc ferrite, J. Mater. Eng. Perform. 14 (2005) 99–103.

[29] Z. Wang, Y. Xie, P. Wang, Y. Ma, S. Jin, X. Liu, Microwave anneal effect on magnetic properties of $Ni_{0.6}Zn_{0.4}Fe_2O_4$ nano-particles prepared by conventional hydrothermal method, J. Magn. Magn. Mater. 323 (2011) 3121–3125.

[30] P. Sivakumar, R. Ramesh, A. Ramanand, S. Ponnusamy, C. Muthamizhchelvan, Preparation and properties of nickel ferrite ($NiFe_2O_4$) nanoparticles via sol–gel auto-combustion method, Mater. Res. Bull. 46 (2011) 2204–2207.

[31] P. Sivakumar, R. Ramesh, A. Ramanand, S. Ponnusamy, C. Muthamizhchelvan, Synthesis and characterization of nickel ferrite magnetic nanoparticles, Mater. Res. Bull. 46 (2011) 2208–2211.

[32] D.L. Zhao, Q. Lv, Z.M. Shen, Fabrication and microwave absorbing properties of Ni–Zn spinel ferrites, J. Alloys Compd. 480 (2009) 634–638.

[33] K. Lagarec D.G. Rancourt, Recoil Mössbauer Spectral Analysis Software for Windows, Version 1.02, Department of Physics, University of Ottawa, Ottawa, ON, 1998.

[34] M.A. Amer, T.M. Meaz, S. Ata-Allah, S. Aboul-Enein, M.O. Abd-El-Hamid, Mössbauer, infrared and X-ray studies of $Ni_{0.5}Zn_{0.5}Cr_xFe_{2-x}O_4$ ferrites, Egypt. J. Solids 28 (2005) 275–293.

[35] L.K. Leung, B.J. Evans, A.H. Morrish, Low-temperature Mössbauer study of a nickel–zinc ferrite: $Zn_xNi_{1-x}Fe_2O_4$, Phys. Rev. B 8 (1973) 29–43.

[36] R.V. Upadhyay, R.G. Kulkarni, Low-temperature Mössbauer study of the Mg–Cd ferrite system, Solid State Commun. 48 (1983) 691–695.

[37] A.M. Sankpal, S.S. Suryavanshi, S.V. Kakatkar, G.G. Tengshe, R.S. Patil, N.D. Chaudhari, S.R. Sawant, Magnetization studies on aluminum and chromium substituted Ni–Zn ferrites, J. Magn. Magn. Mater. 186 (1998) 349–356.

[38] X. Lu, G. Liang, Q. Sun, C. Yang, High-frequency magnetic properties of Ni–Zn ferrite nanoparticles synthesized by a low temperature chemical method, Mater. Lett. 65 (2011) 674–676.

[39] L. Neel, Propriétés magnétiques des ferrites: ferrimagnétisme et antiferromagnétisme. (Magnetic properties of ferrites: ferrimagnetism and antiferromagnétisme.), Ann. Phys. 3 (1948) 137–198.

[40] Z. Peng, X. Fu, H. Ge, Z. Fu, C. Wang, L. Qi, H. Miao, Effect of Pr^{3+} doping on magnetic and dielectric properties of Ni-Zn ferrites by one-step synthesis, J. Magn. Magn. Mater. 323 (2011) 2513.

[41] A. Ghasemi, X. Liu, A. Morisako, Magnetic and microwave absorption properties of $BaFe_{12-x}(Mn_{0.5}Cu_{0.5}Zr)_{x/2}O_{19}$ synthesized by sol–gel processing, J. Magn. Magn. Mater. 316 (2007) 105–108.

[42] D.S. Mathew, R.S. Juang, An overview of the structure and magnetism of spinel ferrite nanoparticles and their synthesis in microemulsions, Chem. Eng. J. 129 (2007) 51–65.

[43] J.M.D. Coey, Rare Earth Permanent Magnetism, John Wiley and Sons, New York, 1996.